

Chapter 2

Experimental Techniques

This section is addressed to briefly describe the main experimental techniques used to study the structural and magnetic properties of the nanoparticles included in this thesis. We first explain the transmission electron microscopy techniques used to explore the morphology and structure of the particles. Then, we introduce two techniques to study the magnetic properties of the samples: SQUID based magnetometry and anomalous hall effect (AHE). Finally, we focus on the description of the synchrotron radiation techniques employed, in particular those based on X-ray absorption mechanisms, which allow studying selectively and locally the structural, electronic and magnetic properties of the nanoparticles systems; these are: X-ray absorption near edge structure (XANES), extended X-ray absorption fine structure (EXAFS), and X-ray magnetic circular dichroism (XMCD).

Later, we will dedicate Chap. 7 to describe the magnetic transverse susceptibility technique, which has been also used to study the magnetic properties of some nanoparticles systems in this dissertation.

2.1 Transmission Electron Microscopy

The transmission electron microscopy (TEM) is a technique whereby an electron beam is transmitted through an ultra thin specimen, forming an image from the interaction between the transmitted electrons and the sample. TEMs are capable of imaging at a significantly higher resolution than light microscopes, owing to the small wavelength of electrons. This enables to examine fine details, even as small as a single column of atoms. This technique usually combines the high resolution imaging with elemental microanalysis and electron diffraction, so that a complete characterization of the shape, size, chemical composition and crystalline structure of nanoparticulate materials is achieved.

In a TEM microscope, an electron gun, located at the top of it, emits the electrons by thermionic or field emission. These electrons travel through vacuum in the column of the microscope where electromagnetic lenses focus them into a very thin beam.

The electron beam then travels through the specimen to study. At the bottom of the microscope, the image is formed on the image plane of objective lens from the unscattered electrons. Then, projector lenses form the images on a screen or CCD camera.

One of the main requirements for this technique is that the sample must be thin enough for electrons to pass through; the interaction between electrons and matter is much stronger than that with visible light, so samples for TEM observation must have thickness below 100 nm. There exists a variety of procedures to prepare samples for TEM observation, depending on the kind of materials and their nature. For example, bulk samples must be first cut to an proper size (~ 3 mm in diameter, 300–400 μm thick); after that, they are thinned, first mechanically and then by ionic or electrolytic milling, until reaching the desired thickness.

Some modern TEMs integrate a high angle annular dark field (HAADF) detector that allows to perform scanning transmission electron microscopy (STEM) measurements. In this mode, the electron beam is focused into a narrow spot that is scanned over the sample in a raster. The rastering of the beam across the sample makes these microscopes suitable for analysis techniques such as mapping by X-ray energy disperse spectrometry (EDX) spectroscopy and electron energy loss spectroscopy (EELS). The HAADF detector collects electrons from an annulus around the beam, forming the image only by very high angle incoherently scattered electrons, as opposed to Bragg scattered electrons in the conventional TEM images. By using a STEM and the HAADF detector, it is possible to form atomic resolution images where the contrast is directly related to the atomic number (Z-contrast image).

The microscopy images and analysis of the magnetic nanoparticles in this work were performed with two TEMs, whose technical specifications are described below.

2.1.1 JEOL JEM 3,000 F

A JEOL JEM 3,000 F Field Emission Microscope has been used by Dr. Luisa Ruiz González and Dr. José María González-Calbet of the Departamento de Química Inorgánica in the Universidad Complutense de Madrid¹ to take some of the images of the nanoparticles systems that we show in this thesis. This microscope is shown in Fig. 2.1a. It operates at acceleration voltages between 100 and 300 kV and it is fitted with an Oxford Instruments energy dispersive X-ray spectrometer (EDS). Its high-resolution performance (a point resolution of 0.17 nm) is then complemented by the ability to perform chemical microanalysis from sub-nanometre areas (below 0.4 nm in some cases). This microscope is equipped with a HAADF detector, so that STEM mode and EELS analysis are also possible.

¹ <http://www.cnme.es/>.

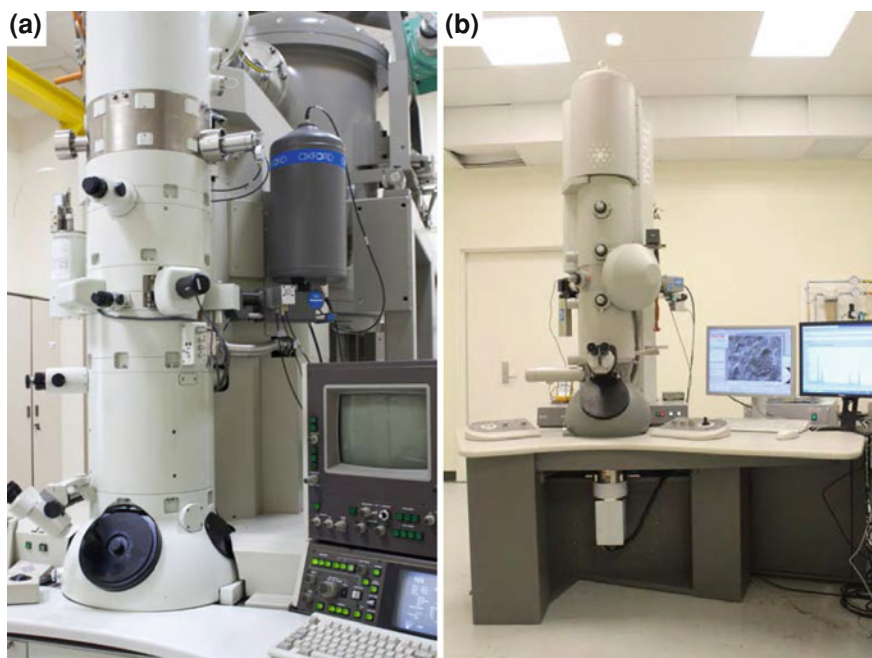


Fig. 2.1 Images of the two models of transmission electron microscopes used to observe the samples. **a** JEOL JEM 3,000 F Field Emission Microscope. **b** FEI Tecnai™ G2 F30 STWIN Field Emission Microscope

2.1.2 FEI Tecnai™ G2 F30 STWIN

Some of the TEM images that we show in this dissertation have taken by Dr. Cesar Magén and Dr. Alfonso Ibarra in a FEI Tecnai™ G2 F30 STWIN Field Emission Microscope of the Laboratorio de Microscopías Avanzadas, Instituto de Nanociencia de Aragón,² Universidad de Zaragoza. A picture of a microscope of this kind is shown in Fig. 2.1b. In this microscope, acceleration voltages as high as 300kV allow reaching a point resolution of 0.2 nm, line resolution of 0.10 nm, and information limit of 0.14 nm. This TEM system is fully loaded including a HAADF detector, EDX, and a Gatan Image Filter (GIF).

2.2 SQUID Based Magnetometry

A magnetometer is an instrument used for the magnetic characterization of a material, by measuring the strength and/or direction of magnetic fields. A superconducting quantum interference device (SQUID) is the most sensitive device available for

² <http://ina.unizar.es/lma/index.html>.

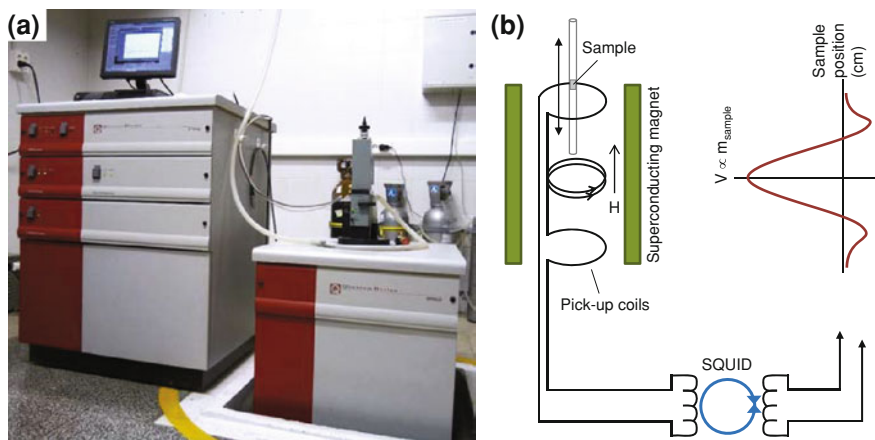


Fig. 2.2 **a** MPMS-XL magnetometer of the Universidad de Zaragoza. **b** Schematics of the SQUID—based measurement system

such purposes. It works as an extremely sensitive current-to-voltage converter, so that, when integrated to a Quantum Design magnetic property measurement system (MPMS), the complete system is a magnetic flux to voltage transducer. The fact of directly measuring magnetic flux is one of the main advantages of SQUID magnetometry, allowing to measure moments on the order of 10^{-7} emu.

A picture of one of the MPMS of the Servicio de Medidas Físicas of the Universidad de Zaragoza,³ which have been used for some of the magnetic characterization described in this manuscript, is shown in Fig. 2.2a. A schematics of the measurement process of a magnetic sample in this equipment is displayed in Fig. 2.2b. In a MPMS, the SQUID does not detect directly the magnetic field from the sample since it may be interfered by any flux from nearby magnetic systems, or even the earth's magnetic field. Instead, a measurement is performed by moving a sample through a system of superconducting pick-up coils, two of them with the same sense very closely spaced, and the other two of the opposite sense, spaced symmetrically outside (see Fig. 2.2b). This system is located outside the sample chamber at the center of the superconducting magnet. As the sample moves through the coils, the magnetic moment of the sample induces an electric current in the detection coils. Because the detection coils, the connecting wires, and the SQUID input coil form a closed superconducting loop, any change of magnetic flux in the detection coils produces a change in the persistent current in the detection circuit, which is proportional to the change in magnetic flux. Since the SQUID is a highly linear current-to-voltage converter, the variation in the current in the detection coils produces corresponding variations in the SQUID output voltage. Based on this profile of voltage (and thus flux) versus position of the sample (see Fig. 2.2b), given the assumption that the signal is from a point dipole, the magnetic moment can be determined.

³ <http://sai.unizar.es/medidas/index.html>.

This MPMS allows measuring magnetization as a function of magnetic fields up to 50kOe, or temperature in a range of 1.9–400 K. AC measurements with a field amplitude of 4Oe and frequencies from 0.01 to 1,000Hz are also possible in this equipment. It integrates a reciprocating sample option (RSO), which consists of a high resolution mode to improve the equipment sensitivity to measure moments as small as 5×10^{-9} emu. Unlike DC measurements where the sample is moved through the coils in discrete steps, the RSO measurements are performed using a servo motor which rapidly oscillates the sample. A digital signal processor (DSP) is incorporated in the RSO, which allows for much more rapid data collection than the standard step scan method. The DSP also decreases the contribution of low frequency noise during data collection, which improves the signal-to-noise ratio resulting in maximum sensitivity.⁴

2.3 Anomalous Hall Effect

The Hall effect [2] (or ordinary Hall effect, OHE) is a well known and studied phenomenon, characterized by the production of a voltage difference (the Hall voltage) across an electrical conductor or semiconductor, transverse to an electric current in the material, and a magnetic field perpendicular to the current. In magnetic materials, there is an additional contribution to the Hall voltage, proportional to the magnetization, called the extraordinary or anomalous Hall effect (AHE). Correlation between the AHE and magnetization enables the use of the Hall voltage measurement for the study of magnetic properties of materials in conditions hardly accessible by other techniques [3].

The Hall voltage in magnetic materials is commonly described by the phenomenological equation [4, 5]

$$V_H = \underbrace{\frac{R_H I}{t} H \cos(\alpha)}_{OHE} + \underbrace{\frac{\mu_0 R_s I}{t} M \cos(\theta)}_{AHE} + \underbrace{\frac{k I}{t} M^2 \sin^2(\theta) \sin(2\phi)}_{PHE} \quad (2.1)$$

where t is the film thickness, R_H , R_s and k are the ordinary, anomalous and planar Hall coefficients, respectively, and the angles α , θ and ϕ are defined in Fig. 2.3. The first term in Eq. 2.1 is the OHE and arises from the Lorentz force acting on conduction electrons. The OHE depends on the z -component of the \vec{H} field, and produces an electric field perpendicular to H_z and the current I . The second term is the AHE and arises due to spin dependent scattering mechanisms. It is associated with a break of the right–left symmetry during the spin–orbit scattering in magnetic materials and its contribution could be much larger than the OHE. The AHE depends

⁴ For further information of SQUID magnetometers see Ref. [1] and/or the Quantum Design website <http://www.qdusa.com/index.html>.

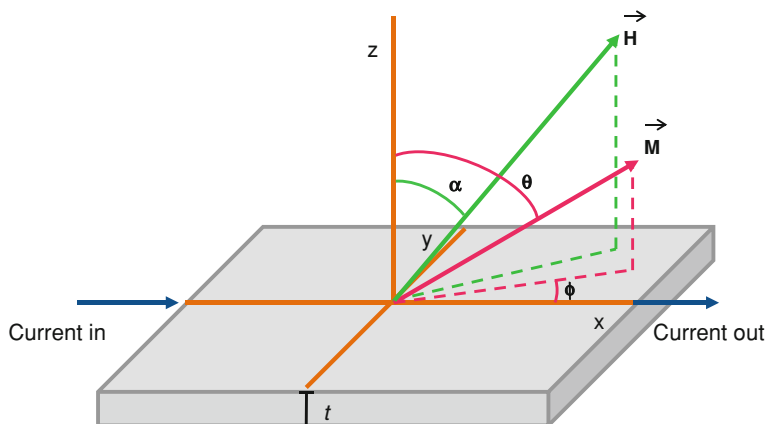


Fig. 2.3 Geometry of the AHE measurement. α is the angle between the applied field and the normal to the sample, θ is the angle between the magnetization and the normal and ϕ is the angle between the current and the in plane component of the magnetization

on the perpendicular component of \vec{M} , and produces an electric field perpendicular to M_z and I . The last term in Eq. 2.1 is the planar Hall effect (PHE), or anisotropic magneto-resistance. The PHE is proportional to the square of the planar component of \vec{M} , and produces an electric field parallel and perpendicular to the current (the one expressed in Eq. 2.1 is perpendicular to the current). Note that all three terms are inversely proportional to the film thickness t . Given this property, the AHE has been recognized as a useful tool for measuring the magnetic hysteresis $M(H)$ loops of thin films, specially those used in perpendicular magnetic recording media (PMRM), ferromagnetic/semiconductor heterostructures (spintronic devices), and diluted-magnetic-semiconductors [4, 5].

The AHE measurements performed on some of the nanoparticles systems described in this thesis were carried out by Dr. Jolanta Stankiewicz in an electrical transport setup of the Departamento de física de la materia condensada and Instituto de Ciencia de Materiales de Aragón (ICMA), CSIC—Universidad de Zaragoza, and in a Quantum Design Physical Property Measurement System (PPMS) of the Servicio de Medidas Físicas of the Universidad de Zaragoza.⁵

2.4 X-ray Absorption Spectroscopies in Synchrotron Radiation Facilities

Several experimental techniques based on interactions of radiation with matter require of highly intense, bright, continuous and tuneable light sources [6, 7]. These requirements are easily fulfilled with synchrotron radiation sources. These large-scale

⁵ <http://sai.unizar.es/medidas/index.html>.

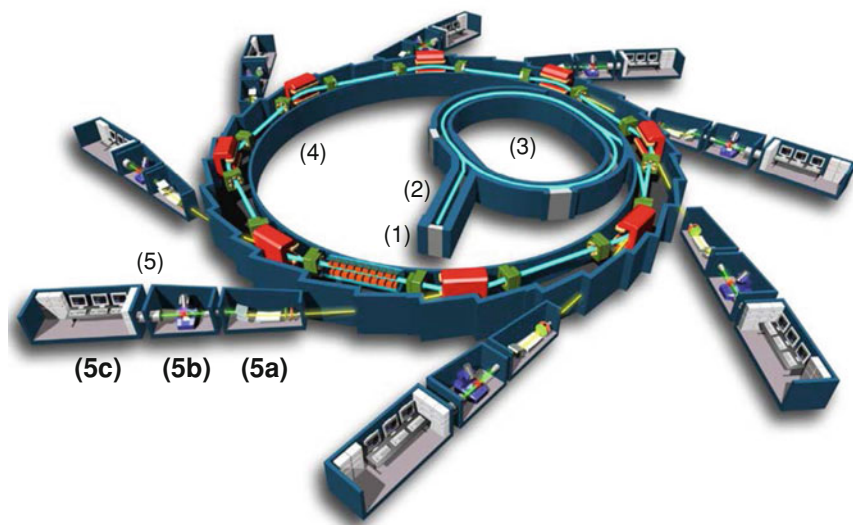


Fig. 2.4 General diagram of a synchrotron facility. 1 Electron or proton gun, 2 LINAC, 3 booster, 4 storage ring, 5 beamline, 5a optics cabin, 5b experimental hutch, and 5c control cabin

facilities consist of particle accelerators that speed up charged particles, such as electrons or protons, into an orbit at almost the speed of light. According to the electromagnetic theory, an electric charge irradiates energy when accelerated. This radiation is emitted tangentially to the circular trajectory of the electric charge when it is deflected. Third generation synchrotron radiation facilities are the most powerful currently operating synchrotron light sources, and have become one of the essential tools for basic and applied scientific research over the world.

The main properties of the synchrotron light may be summarized as follows: it has a broad spectrum from microwaves to hard X-rays, so that it is a tuneable radiation source; its high intensity photon beam of about 10^{18} – 10^{20} photons/s/mm² (compared to the 10^8 photons/s/mm² of a conventional X-ray tube) allows rapid experiments; it is a highly brilliant photon beam generated by a small divergence and small size source (spatial coherence); it is a very stable (submicron source stability) and polarized radiation.

A diagram of a synchrotron radiation facility is shown in Fig. 2.4. The synchrotron light generation starts in an electron (or proton) gun (1), where a cathode produces free electrons released to a linear accelerator or LINAC (2). The LINAC feeds a booster ring (3), where electrons receive a boost in energy from approximately 250 MeV to approximately 1.5–8 GeV from microwaves generated in a radio frequency cavity as they circulate in the ring. The booster increases the speed of the electrons close to the speed of light. When the electrons have enough energy to produce light, an injection system transfers them from the booster ring to the storage ring (4): a tube

with straight and circular sections kept in ultra high vacuum, with quadrupole and sextupole magnets designed to focus the electron beam. Once there, the electrons will circulate for a long period of time producing photons every time the dipole magnets (also called bending magnets) change the direction of the flow of electrons. After each turn there is a photon port to allow the light to travel down the beamlines to the research stations. Aside from the bending magnets, synchrotron light may also be produced by insertion devices, such as wigglers or undulators, located at the straight sections of the storage ring. They consist of periodic magnetic structures that stimulate highly brilliant, forward-directed synchrotron radiation emission by forcing the stored charged particle beam to perform wiggles, or undulations, as they pass through the device. The magnet arrays are designed in such a way that the emitted radiation interferes constructively to produce a very intense and concentrated beam in narrow energy bands in the⁶ spectrum.

Each beamline has an optics cabin (5a), an experimental hutch (5b), and a control cabin (5c). The optics cabin has optical instruments used to tailor the type of radiation to have the characteristics for each experiment. The experimental hutch contains the support mechanism, and the environment for the sample study. Different instruments and detectors record the information produced from the interaction of the synchrotron light and the sample. The control cabin allows the researchers to control the experiments and collect the data.

The synchrotron radiation source used to study the magnetic nanoparticles in this dissertation is the European Synchrotron Radiation Facility (ESRF),⁷ which is a third generation and the most powerful synchrotron in Europe. It is located in Grenoble, France. It operates at a nominal energy of 6 GeV, with a circumference of 844 m, and around 49 operating beamlines.

X-ray absorption spectroscopy (XAS) is one of those techniques that is best performed with the intense and tunable X-ray beams produced in a synchrotron radiation source. This spectroscopy refers to the details of how X-rays are absorbed by an atom at energies near and above the core-level binding energies of that atom. The absorbing process is illustrated in Fig. 2.5a. An X-ray photon reaches the absorbing atom (in blue) and disappears. After the interaction, a photoelectron is emitted. Depending on the energy of the incident X-ray photon, different processes occur. If the binding energy of certain electron in the absorbing atom is equal to the X-ray photon energy, there is a sharp increase in the absorption cross-section, called absorbing edge, corresponding to an emission of the photoelectron to the continuum states, as indicated in 2.5b. The absorption edges are named according to the principle quantum number of the electron that is excited: K for $n = 1$, L for $n = 2$, M for $n = 3$, and so on. The energies at which edges appear are unique for each element, fact that makes this spectroscopy an element-selective technique.

⁶ General diagram of Synchrotron Soleil with Copyright ©EPSIM 3D/JF Santarelli.

⁷ <http://www.esrf.eu/>.

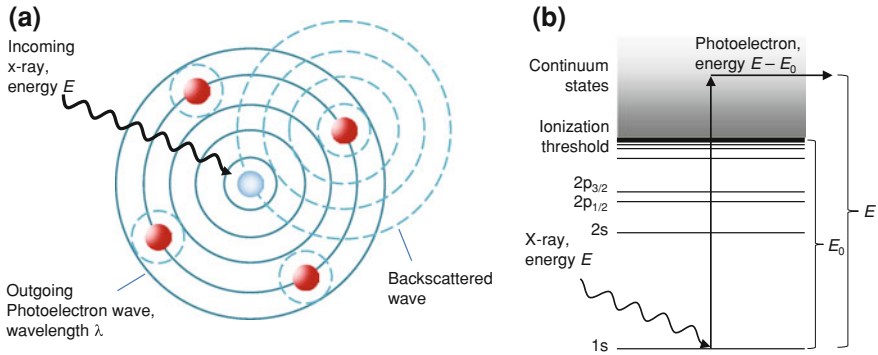
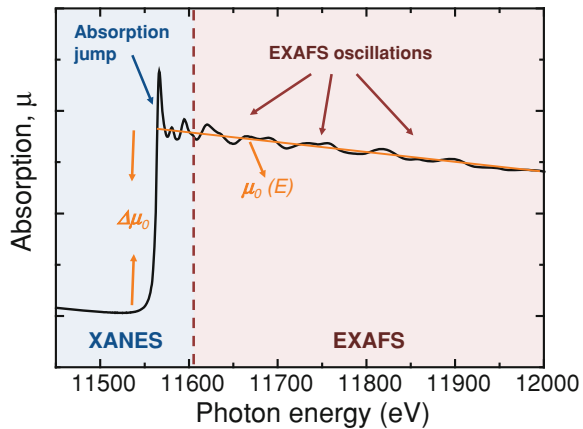


Fig. 2.5 Schematics of the X-ray absorption process. **a** An absorbing atom (blue) is shown here surrounded by several other atoms (red). Whenever the energy of an X-ray is greater than the binding energy of one of the absorbing atom's core electrons, a photoelectron is liberated. **b** Energy-level diagram of an absorbing atom showing the atom's first few core-electron orbitals: $1s$, $2s$, $2p_{1/2}$, and $2p_{3/2}$. The ionization potential energy is denoted by E_0 . With the absorption of a photon of energy E , the electron undergoes a transition to an unbound state in the continuum and, by conservation of energy, acquires a kinetic energy ($E - E_0$) [8]

Fig. 2.6 XAFS spectrum recorded at the Pt L_3 edge for a Pt foil at 300 K. We have divided the spectrum into its two main regions: XANES—X-ray Absorption Near Edge Structure, and EXAFS—Extended X-ray Absorption Fine Structure. The background function μ_0 , and the measured jump at the absorption threshold energy E_0 , $\Delta\mu_0$, are also shown



2.4.1 X-ray Absorption Fine Structure

X-ray absorption fine structure (XAFS) is a specific structure observed in XAS [8, 9]. A usual XAFS spectrum can be seen in Fig. 2.6, where the two spectral regions are identified: the near-edge region XANES, typically within 50 eV of the main absorption edge, and the extended fine-structure (EXAFS) which spans the 50–2,000 eV above the edge. The basic physical description of these two regimes is the same. EXAFS results from the interference in the single scattering process of the photoelectron scattered by surrounding atoms (see Fig. 2.5a), and it provides

information on the local structure such as distances between neighbors, thermal and structural disorder in a material. Information on the geometry of the local structure is provided by the analysis of the multiple scattering peaks in the XANES spectra. However, XANES is harder to be described in a quantitative way since there is not an equation to parameterize this region, while it does exist for EXAFS, as it will be described below.

The X-ray absorption process is a transition between two quantum states: from an initial state with an X-ray, a core-electron, and no photoelectron, to a final state with no X-ray, a core-hole, and a photoelectron. According to the Fermi's golden rule for dipolar transitions (following the dipole selection rules $\Delta l = \pm 1$ and $\Delta s = 0$), the transition probability between two electronic states, per unit time, is defined as

$$W_{if} = \frac{2\pi}{\hbar} \left(\frac{eE_0}{2} \right)^2 |\langle i | \hat{\epsilon} \cdot \vec{r} | f \rangle|^2 \rho(E_f) \quad (2.2)$$

where $\rho(E_f)$ is the density of final states, $\langle i |$ is the initial state of the core-electron, $|f\rangle$ the final state of the photoelectron, and $\hat{\epsilon} \cdot \vec{r}$ the dipole operator. Since the core-level electron is very tightly bound to the absorbing atom, the initial state will not be altered by the presence of the neighboring atom. The final state, on the other hand, will be affected by the neighboring atom because the photoelectron will be able to see it. The absorption coefficient $\mu(E)$ is proportional to the sum of possible final states f of the transition probability in Eq. 2.2. It is calculated according to the first order approximation of the time-dependent perturbation theory, based on the interaction between the electromagnetic field and the atom potential.

In the EXAFS region, the spectrum reflects oscillatory variation of the X-ray absorption coefficient, $\mu(E)$, as a function of photon energy, E , beyond the absorption edge (see Fig. 2.6). We define the EXAFS fine-structure function $\chi(E)$ as

$$\chi(E) = \frac{\mu(E) - \mu_0(E)}{\Delta\mu_0(E)} \quad (2.3)$$

where $\mu(E)$ is the measured absorption coefficient, $\mu_0(E)$ is a smooth background function representing the absorption of an isolated atom, and $\Delta\mu_0(E)$ is the measured jump in the absorption $\mu(E)$ at the threshold energy E_0 . These parameters are also represented in Fig. 2.6.

According to the described absorption process, the EXAFS $\chi(E)$ is proportional to the amplitude of the scattered photoelectron at the absorbing atom. Therefore, EXAFS is best understood in terms of the wave-like nature of the photoelectron created in this process. Thus, it is common to convert the X-ray energy to k , the wave number of the photoelectron, being $k^2 = 2m(E - E_0)/\hbar^2$, and m the electron mass. **The primary quantity for EXAFS is then $\chi(k)$, the oscillations as a function of photoelectron wave number.** To emphasize the oscillations, $\chi(k)$ is often weighted by a power of k , typically k^2 or k^3 . The different frequencies composing these oscillations correspond to different near-neighbor coordination shells, described and modeled according to the EXAFS equation

$$\chi(k) = \sum_j \frac{N_j S_0^2 F_j(k) \exp(-2k^2 \sigma_j^2) \exp\left(-\frac{2R_j^2}{\lambda_j(k)}\right)}{k R_j^2} \sin(2k R_j + \delta_j(k)) \quad (2.4)$$

where $F_j(k)$ is the backscattering amplitude from each of the N_j neighboring atoms, $\delta_j(k)$ is the total phase shift experienced by the photoelectron, R_j is the distance to the neighboring atom j , σ_j^2 is the disorder in the neighbor distance, parameter usually known as Debye–Waller factor, and S_0^2 is the amplitude reduction due to many-body effects. The term $\exp(-2R_j^2/\lambda_j(k))$ is due to inelastic losses in the scattering process, with λ_j being the electron mean free path. The EXAFS equation allows us to determine N , R , and σ^2 knowing the scattering amplitude $F(k)$ and phase-shift $\delta(k)$ for each path. Furthermore, since these scattering factors depend on the atomic number, Z , of the neighboring atom, EXAFS is also sensitive to the atomic species of the neighborhood.

The EXAFS $\chi(k)$ is usually Fourier transformed into a radial structure function $\chi(R)$ that represents the data in terms of distances from the absorber. Peak positions in this radial structure function roughly correspond to the radii of the scattering shells.

2.4.1.1 BM29 Beamline at the ESRF

The XAFS experiments on the magnetic nanoparticles system studied here were performed in collaboration with Dr. Sakura Pascarelli at the general purpose X-ray absorption spectroscopy beamline BM29 [10] at the ESRF.⁸ This beamline is devoted to carry out XAFS experiments at a very large operational energy range with reasonable X-ray flux: 4–74 keV, coming from a bending magnet. It has a high energy resolution, typically a factor 3–5 better than the intrinsic spectral broadening at any K or L absorption edge; a high spectral signal to noise ratio, above 7.0×10^4 for well prepared samples; a high beam stability; and a high level of automation.

A schematic diagram of a conventional XAFS beamline, as BM29, is shown in Fig. 2.7. The full spectrum of synchrotron light passes through an entrance slit, which helps collimate the radiation before entering into a double-crystal monochromator. The X-rays diffract off the crystals' lattice planes, which are aligned at an angle θ with respect to the incoming beam. Because of the Bragg scattering condition $n\lambda_j = 2d \sin \theta$, only X-rays of energy $E_n = nhc/\lambda_j$ can reflect off the crystals. Different X-ray energies can be selected by changing the angle θ of the crystals. The monochromatic beam passes through an ion chamber that monitors the beam intensity I_0 by absorbing part of it. The beam then passes through the sample, and the intensity of the transmitted X-ray I is measured by a second ion chamber. Taking the log of the ratio of I/I_0 yields the absorption. We can also determine the sample's absorption by measuring the intensity of its X-ray fluorescence, I_f with a detector

⁸ In a recent upgrade, performed in 2011, the ESRF BM29 beamline has been relocated to the BM23 port, which is the one currently operational. For further information see <http://www.esrf.eu/UsersAndScience/Experiments/ElectStructMagn/BM23/>.

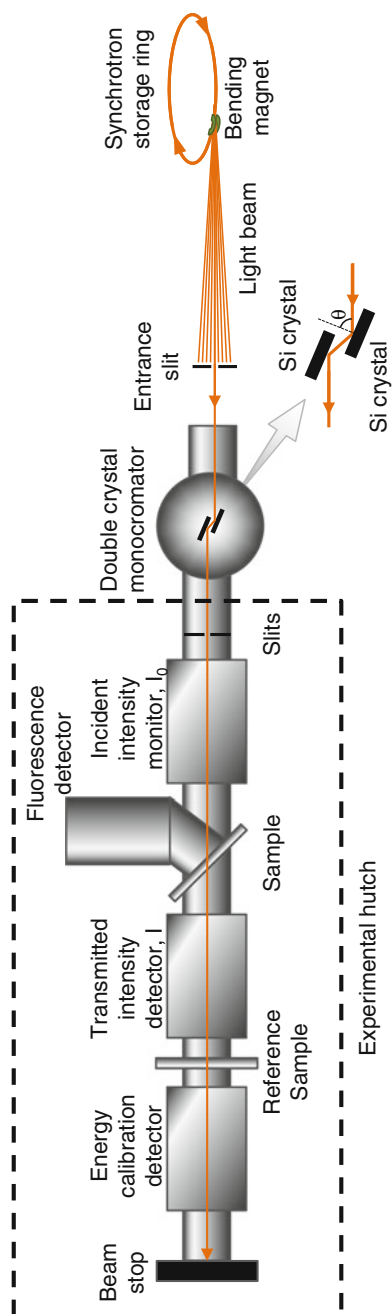


Fig. 2.7 Diagram of the assembly used in a conventional measurement of XAFS

that is out of the beam path, usually oriented at 45° with respect to the sample. Finally, the beam passes through a reference sample whose absorption edge is used to help correct for uncertainties in the beam's energy.

2.4.2 X-ray Magnetic Circular Dichroism

Some synchrotron radiation techniques take advantage of the natural polarization of this light in the plane of the electron orbit in order to perform polarization-dependent measurements. This is the case of the X-ray magnetic circular dichroism (XMCD), where the difference between two X-ray absorption spectra recorded in a magnetic field, one measured with right circularly polarized light (+1 helicity), and one with left circularly polarized light (−1 helicity), is performed. The XMCD is then defined as

$$XMCD(E) = \mu^- - \mu^+ \quad (2.5)$$

where μ^- and μ^+ are the absorption coefficients with left and right circularly polarized light, respectively. The differences in the absorption of light with opposite helicities arise from an additional dipole selection rule for dipolar transitions, $\Delta m_j = \pm 1$ for +1 and −1 helicity, respectively, in Eq. 2.2; the dipole operator, $\hat{\epsilon} \cdot \vec{r}$, must also be expressed as dependent of the light polarization. This way, **XMCD reflects the difference in the density of empty states with different spin moment**, so that by closely analyzing the XMCD signal, information can be obtained on the magnetic properties of the absorbing atom, such as its spin and orbital magnetic moment.

In a simple atomic monoelectronic picture, the XMCD occurrence may be understood in terms of the two-step approach described by Schütz et al. [11]. Let us first consider an X-ray photon with helicity +1 absorbed by an electron from a spin-orbit-split core-level, for example, $2p_{3/2}$ (L_3 edge) and $2p_{1/2}$ (L_2 edge), as illustrated in Fig. 2.8a. When absorbing a circularly polarized photon, some of the orbital moment of the photon can be transferred via the spin-orbit coupling to the electron spin. This results in an effective spin polarization of the excited electrons, process known as Fano-effect [12]. From the $2p_{3/2}$ state, 62.5 % of excited electrons carry a spin of $m_s = +1/2$ and only 37.5 % of $m_s = -1/2$. From the $2p_{1/2}$ state, 75 % of excited electrons carry a spin of $m_s = -1/2$ and only 25 % of $m_s = +1/2$. Note that the sign of spin polarization is different for the different $2p$ states, provided their different spin-orbit coupling: $(l + s)$ at the $p_{3/2}$ -state, and $(l - s)$ at the $p_{1/2}$ -state. If there were no spin-orbit-splitting, that is, no energy gap between $2p_{3/2}$ and $2p_{1/2}$ states, the averaged spin polarization would be zero.

With this spin and orbital polarized excited electrons, the polarization of the unoccupied final states is probed in the second step of this model. Any imbalance in either spin or orbital momentum in the final states will give rise to a dichroic effect. Thus, in a magnetic material, the exchange splitting leads to a splitting of the valence band, lowering the energy for electrons with one spin orientation (majority electrons) and rising it for the other (minority electrons), as illustrated in Fig. 2.8a. The transition

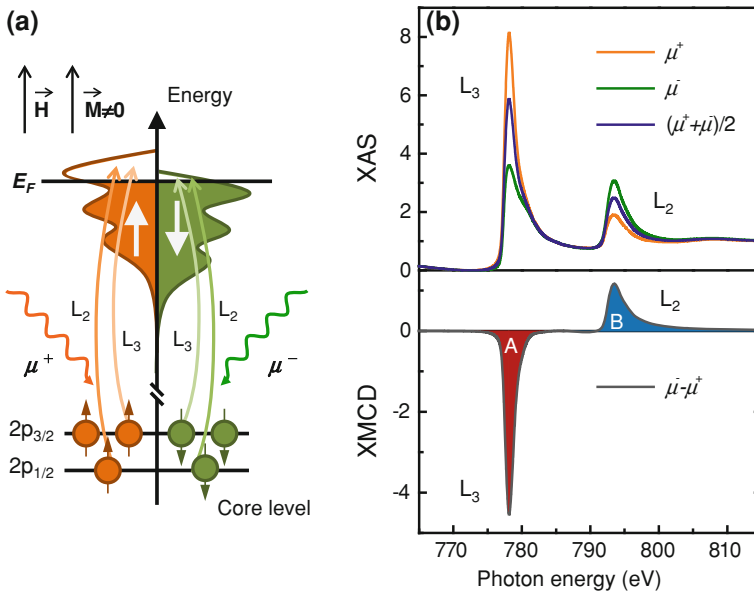


Fig. 2.8 **a** Diagram of the simple mono-electronic two-step picture of the resonant excitation process in a magnetic material, resulting in a XMCD signal. First a circularly polarized photon excites a spin polarized electron (Fano-effect) from a $2p$ level; this spin polarized electron is used in step two to probe the spin polarized occupation levels of the $3d$ states. **b** XAS spectra and XMCD signal at the Co $L_{2,3}$ in a system of Co-Pt NPs. In this case, a scan over the $2p$ absorption edges of Co with circularly polarized light leads to non-statistic absorption lines due to differently spin occupied $3d$ states. This effect is reversed by inverting either the magnetization (change of the magnetic field direction) or the light polarization. In this picture the polarization of the light is reversed between the orange and green absorption curves. The difference of left and right circularly polarized scan is the dichroic signal displayed below

probability of electrons in a dipole transition are proportional to the unoccupied density of states, as expressed in Eq. 2.2. If this density of states is different for different spin orientations and the electrons are spin polarized, the absorption spectra will change when the spin polarization is inverted, as due to the change of the helicity of the incoming light. This results in spectra as the one represented in Fig. 2.8b, where we have plotted the XAS recorded with right and left circularly polarized X-rays at the Co $L_{2,3}$ edges in a Co-Pt NPs sample, along with the resulting XMCD signal.

To see this effect it is required that the magnetization of the sample has at least a component parallel to the incoming light. The inversion of the magnetization has the same effect on the absorption process as the inversion of the photon polarization. Thus, XMCD measurements can be performed in those two equivalent ways: either by changing the helicity while keeping constant the applied magnetic field, or by changing the direction of the magnetic field at a constant helicity of the light.

XMCD became more powerful as a tool for the element-selective characterization of magnetic materials with the derivation of the magneto-optical sum rules by Thole

et al. [13] and Carra et al. [14] for spin-orbit split absorption edges. Via these sum rules it is possible to determine both the spin, $m_S = -2\mu_B \langle S_z \rangle / \hbar$, and orbital, $m_L = -\mu_B \langle L_z \rangle / \hbar$, magnetic moments in the atom being probed with the XMCD measured at its $L_{2,3}$ edges. In order to write the sum rules, let us define the following integrals

$$\begin{aligned} A &= \int_{L_3} (\mu^- - \mu^+) dE \\ B &= \int_{L_2} (\mu^- - \mu^+) dE \\ C &= \int_{L_3+L_2} (\mu^- + \mu^+ + \mu^0) dE \end{aligned} \quad (2.6)$$

which follow the symbols and sign criteria denoted in Ref. [15]. The absorption spectrum μ^0 requires in principle linearly polarized radiation, but is usually approximated by $\mu^0 = 1/2(\mu^+ + \mu^-)$. Before application of the sum rules it is necessary to separate the absorption intensity due to the electron transitions we are interested in. Thus, the C integral must be calculated after removing the unwanted transitions into higher unoccupied states or into the continuum in the absorption spectra. It is usually performed by subtraction of a hyperbolic step function with one step at the L_3 and one at the L_2 edge [16]. If there are less pronounced absorption maxima at the absorption edges, a reference spectrum of a similar element with a well-known number of unoccupied states should be subtracted.

The sum rule for the orbital moment per unoccupied final state n_h is expressed as

$$\frac{m_L}{n_h} = -\frac{2(A+B)}{C} \mu_B \quad (2.7)$$

For the spin sum rule, it is usual to define the *effective* spin moment, $m_{\text{Seff}} = m_S + m_D$, which considers the dipolar term m_D . The latter is expressed as a function of the expectation value of the intra-atomic magnetic dipole operator $\langle T_z \rangle$ [15, 17], as $m_D = -7\langle T_z \rangle \mu_B / \hbar$, which reflects the asphericity of the spin moment distribution around the absorbing atom. In order to determine m_S , one option is to assume that the angle averaged $\langle T_z \rangle$ is much smaller than the spin moment and can be neglected, as in the case where the absorbing atom is in a cubic (undistorted) symmetry. On the contrary, for lower symmetries or distorted systems, $\langle T_z \rangle$ may be obtained from angle dependent experiments or theoretically approximated [17, 18]. For example, for non-cubic structures, $\langle T_z \rangle$ might have a maximum value of $\langle S_z \rangle / 3$, corresponding to the Lorentz local field at the absorbing atom site [19]. However, the angle average of $\langle T_z \rangle$ with this approximation in the whole sample usually cancels out, as well.

If the angle average of $\langle T_z \rangle$ is zero, $m_{\text{Seff}} = m_S$, and the spin moment, also per n_h , is written as

$$\frac{m_S}{n_h} = -\frac{3(A - 2B)}{2C} \mu_B \quad (2.8)$$

Therefore, the orbital to spin moment ratio is defined as

$$\frac{m_L}{m_S} = \frac{4(A + B)}{3(A - 2B)} \quad (2.9)$$

which is independent of n_h and the C integral. For a precise estimation of these moments, one must separate the L_3 and the L_2 contribution of the spectrum, which is fairly easy for the heavier $3d$, and for $4d$ and $5d$ elements since the spin-orbit split increases with the nuclear charge of the atom. Additionally, one needs to know the exact amount of d -holes in the material, for which no straight forward experimental determination procedure exists. This drawback may be solved by either obtaining the number of d -holes from band structure calculations, or by expressing the sum rules results as magnetic moments per d -hole.

2.4.2.1 ID08 and ID12 Beamlines at the ESRF

The XMCD experiments on the magnetic nanoparticles studied here were performed at the ID08 beamline (for soft X-rays ranging between 0.3 and 1.6 keV) in collaboration with Dr. Peter Bencok and Dr. Nick Brookes, and at the ID12 beamline (for hard X-rays ranging between 2 and 20 keV) in collaboration with Dr. Fabrice Wilhelm, Dr. Alevtina Smekhova and Dr. Andrei Rogalev, in the ESRF.⁹ These beamlines are dedicated to polarization-dependent X-ray absorption and excitation spectroscopies. Both beamlines make use of undulators to produce the polarized light for XMCD measurements. By longitudinal phasing of the magnetic arrays, the polarization of the undulator emission can be changed from linear to elliptical and circular. They complement each other to probe magnetism in a diverse range of systems with X-ray magneto-optical techniques and to study the electronic structure of materials X-ray and photoelectron emission techniques.

ID08 is equipped with two APPLE II undulators providing $\sim 100\%$ circular/linear beam polarization, a spherical grating monochromator with an energy resolution close to $\Delta E/E = 5 \times 10^{-4}$ at 850 eV, optics focussing down to 6–40 [60–500] microns (FWHM) vertical [horizontal] beam size, and several different UHV experimental stations and sample preparation facilities. ID12 has three helical undulators installed on the its straight section: HELIOS-II, APPLE-II and the so-called “ElectroMagnet/Permanent magnet Hybrid Undulator” (EMPHU) that have been optimized to complement one another. They give ID12 the advantages of fully control of the polarization state of the incident X-ray beam over a wide

⁹ For further information about ID08 and ID12 beamlines, please visit <http://www.esrf.eu/UsersAndScience/Experiments/ElectStructMagn>.

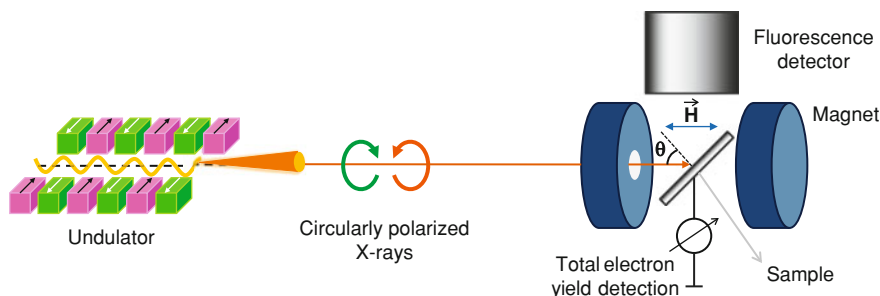


Fig. 2.9 Basic diagram of the XMCD measurement setup at ID08 and ID12

energy range. ID12 uses a double-crystal monochromator with a resolution of $\Delta E/E = \sim 10^{-4}$ to select the energy of the polarized X-rays for experiments.

A schematic of the basic setup for XMCD experiments in these two beamlines is shown in Fig. 2.9. The polarized and monochromatized X-rays are directed through the sample, which is located at the center of a superconducting magnet. The magnetic field is applied on the direction of the incoming beam. The detection of the polarized dependent X-ray absorption spectra may be performed by fluorescence yield (FY) or total electron yield (TEY), the latter regularly used in the soft X-ray regime. The fluorescence detectors are (single- or multi-anode) ion implanted silicon photodiodes, which are characterized by a high efficiency in the X-ray range, fast time response, excellent linearity, and nearly insensitivity to magnetic fields.

References

1. R. C. Black, F. C. Wellstood *Measurements of Magnetism and Magnetic Properties of Matter*, Chapter 12, (Wiley, New York, 2006), pp. 391–480
2. E.H. Hall, On a new action of the magnet on electric currents. *Am.J. Math.* **2**(3), 287–292 (1879)
3. A. Gerber, A. Milner, M. Karpovsky, B. Lemke, H.-U. Habermeier, J. Tuaillon-Combes, M. Négrier, O. Boisson, P. Mélinon, A. Perez, J. Magn. Magn. Mater. **242–245**, 90–97 (2002)
4. J. Lindemuth, B. Dodrill, *IEEE Trans. Magn.* **40**, 2191 (2004)
5. N. Nagaosa, J. Sinova, S. Onoda, A.H. MacDonald, N.P. Ong, Anomalous hall effect. *Rev. Mod. Phys.* **82**, 1539–1592 (2010)
6. J.M. Hollas, *Modern Spectroscopy* (Wiley, New York, 2004)
7. M. Hof, *Basics of Optical Spectroscopy* (Wiley-VCH Verlag GmbH & Co. KGaA, Weinheim, 2005), pp. 37–47
8. S. Conradson, XAFS. A technique to probe local structure. *Los Alamos Sci.* **26**, 422 (2000)
9. M. Newville, *Fundamentals of XAFS* (University of Chicago, Chicago, 2004)
10. A. Filipponi, M. Borowski, D.T. Bowron, S. Ansell, A. Di Cicco, S. De Panfilis, J.P. Itie, *Rev. Sci. Instrum.* **71**, 2422 (2000)
11. G. Schütz, M. Knülle, R. Wienke, W. Wilhelm, W. Wagner, P. Kienle, R. Frahm, *Z. Phys. B Condens. Matter.* **73**(1), 67–75 (1988)
12. U. Fano, Spin orientation of photoelectrons ejected by circularly polarized light. *Phys. Rev.* **178**, 131–136 (1969)

13. B.T. Thole, P. Carra, F. Sette, G. vander Laan, Phys. Rev. Lett. **68**, 1943 (1992)
14. P. Carra, B.T. Thole, M. Altarelli, X. Wang, Phys. Rev. Lett. **70**, 694 (1993)
15. J. Stohr, J. Electron Spectrosc. Relat. Phenom. **75**, 253 (1995)
16. C.T. Chen, Y.U. Idzerda, H.-J. Lin, N.V. Smith, G. Meigs, E. Chaban, G.H. Ho, E. Pellegrin, F. Sette, Phys. Rev. Lett. **75**, 152 (1995)
17. J. Stohr, Phys. Rev. Lett. **75**, 3748–3751 (1995)
18. C. Piamonteze, P. Miedema, M.F. de Groot, Accuracy of the spin sum rule in XMCD for the transition-metal L edges from manganese to Copper. Phys. Rev. B **80**, 184410 (2009)
19. V.V. Krishnamurthy, D.J. Singh, N. Kawamura, M. Suzuki, T. Ishikawa, Phys. Rev. B **74**, 064411 (2006)

Magnetic Nanoparticles

A Study by Synchrotron Radiation and RF Transverse
Susceptibility

Figueroa, A.I.

2015, XI, 165 p. 85 illus., 2 illus. in color., Hardcover

ISBN: 978-3-319-07093-3